 Conference ID: 1570790231

Portable Multi-Wavelength Fluorescence Measurement Device: Empirical Evaluation

Raphael Hagen, Daniel Fehr, Fabrizio Spano, Samuel Babity, Davide Brambilla, Mathias Bonmarin

***Abstract*—Monitoring-based preventive medicine relies heavily on minimal or noninvasive, portable, and cost-effective measurement solutions. In this study, we present a handheld multi-wavelength fluorescence measurement system for detection of dermally injected fluorescent tracers. The circular detection area of the device is positioned on the sample containing the fluorescent marker. The marker is excited at regular intervals by a pulse of light. The optical output power is controlled by a laser diode driver, which receives direct feedback on the emitted light intensity from the monitor photodiode integrated into the laser diode package. An optical diffuser is located in front of each laser diode to ensure uniform illumination of the measurement area. Pulsed excitation of the fluorescent tracer allows alternate measurement of foreground and background light intensity. By subtracting the background from the foreground and using a switched-input photocurrent measurement technique, the measured photocurrent represents the actual light emission from the marker. The instrument has interchangeable modules that contain the excitation electronics and emission filter. These modules allow the instrument to be configured for a variety of different fluorescent markers. In vitro measurements show that the device is capable of performing fluorescence measurements for its intended use as a point-of-care device in preventive medicine.**

***Index Terms*—Fluorescence meter, fluorometer, portable, handheld, multi-wavelength, ratiometric fluorescent tattoo**

I. Introduction

HEALTH care systems have traditionally focused on treating patients with clinical symptoms of disease. The rising cost of treating long-term and chronic conditions has led to a shift in emphasis to preventive medicine. Preventive medicine relies heavily on monitoring and proactive detection of subclinical decline. As a result, there is a growing need for measurement systems that provide rapid and reliable information outside of a clinical setting [1], [2]. Recent work has demonstrated that ratiometric fluorescent tattoos administered via microneedles can be used to monitor physiological and pathological conditions [3], [4]. By quantifying the amount administered using fluorescence intensity measurements, this approach could be universally used to detect and monitor a variety of conditions.

Poor biocompatibility, high cost, device size, and limitation to low-wavelength fluorescence hinder universal application of existing fluorescence measurement systems in preventive medicine [5]–[14].

In this paper, we describe a first example of a handheld multi-wavelength fluorescence sensor for detection of various fluorescent markers. The proposed system allows measurement of fluorescence intensity in a portable and less expensive package than existing devices, while maintaining the sensitivity required for clinical use. To achieve this, optical and electronic design decisions must be thoroughly considered. For specific tattoo detection and monitoring, a circular measurement area of 30 mm diameter must be imaged on the skin. The initial version of the instrument allows measurement of Cy3, Cy5, and Cy7.5 fluorescent probes, but offers the possibility of expansion to other fluorescent markers. This requires a system that allows quick and easy adaptation to the specific requirements of each marker to be measured. With the goal of full portability, the instrument must support either a commercially available power adapter or a mobile power source such as a power bank. To keep development costs low and enable rapid prototyping, efforts must be made to design the device's housing using standard fused deposition modeling (FDM) 3D printing techniques.

This paper is an extension of the proceedings "Portable Multi-Wavelength Fluorescence Measurement Device" published at the 2022 IEEE International Symposium on Medical Measurements and Applications [15].

II. Principle of Operation

The multi-wavelength fluorescence meter is a handheld, battery-operated fluorescence measurement system. It is based on the principles of non-imaging optics, i.e., there is no need to create an image of an object, the optical system rather transforms the radiation from the source to the receiver. In the case of the present application, the source is represented by the excited ratiometric fluorescence tattoo, and the receiver is a photodiode that converts the optical signal into an electrical one.

A. Excitation

A fluorescent marker is most efficiently excited by light at a specific wavelength, the excitation maximum. At the excitation maximum, the photon absorption of the marker is greatest and thus produces the greatest fluorescence output (emission). Emission is similar: emission is most likely to occur at a specific wavelength, the emission maximum. The excited fluorescent label also emits light near the emission maximum, but with lower intensity. The wavelength-dependent excitation and emission intensity of a particular marker is represented by

R.H., D.F., F.S. and M.B. gratefully acknowledge financial support from the ZHAW School of Engineering. S.B. and D.B. gratefully acknowledges financial support from the Faculty of Pharmacy at the Université de Montréal, the Natural Sciences and Engineering Research Council of Canada (Discovery program (RGPIN-2018-05076) and the Alexander Graham Bell Canada Graduate Scholarship), the Fonds de Recherche du Québec (Doctoral Research Scholarship), and the Canadian Generic Pharmaceutical Association and Biosimilars Canada.

This article has been accepted for publication in IEEE Transactions on Instrumentation and Measurement. This is the author's version which has not been fully edited and content may change prior to final publication. Citation information: DOI 10.1109/TIM.2023.3270999 Conference ID: 1570790231

its respective spectra. In Fig. 1, the emission and absorption spectra of Cy3, Cy5, and Cy7.5 are shown. Illumination at a wavelength lower or higher than the excitation maximum affects only the emission intensity of the light emitted by the marker. The overall range and shape of the emission spectra remain unchanged [16]. Therefore, it is desirable to excite near the excitation maximum of the marker and capture the emitted light over as wide a range as possible in the emission spectra.

Of the many light sources available, edge-emitting laser diodes are best suited for this application. Unlike many other light sources, laser diodes emit monochromatic radiation, so no monochromator or excitation filter is required, reducing both cost and complexity. Laser diodes with emission wavelengths from approximately 405 to 1500 nm are available in a variety of packages and optical power categories, providing a wide range of laser diodes to choose from.

To excite different fluorescent labels, a compatible laser diode must be selected for each. A laser diode is considered compatible if its typical emission wavelength is near the excitation maximum of the marker, as shown in Fig. 1. The emission spectrum of the laser diode is subject to a slight red shift as a function of operating temperature. Therefore, it is crucial to operate the laser diode in a temperature window where the induced red shift is negligible. More specifically, this means that changes in operating temperature will only minimally alter the excitation efficiency and will not affect the separation of laser diode excitation and marker emission. This is especially important since the excitation pulse from the laser diode is orders of magnitude stronger than the emission from the marker. If only a small portion of the excitation light is detected by the photodiode, the measurement will be distorted. Therefore, the instrument continuously monitors the temperature of the laser diode and prevents or aborts measurements when a certain temperature threshold is exceeded. The temperature threshold depends on the type of laser diode and must be calibrated beforehand. This is done by measuring the emission spectra of the laser at different operating temperatures. It was found that the emission spectra of the laser diode (RLT635-50MGS, Roithner Lasertechnik GmbH, Austria) used for Cy5 excitation and the laser diode (QL78M6SA, Roithner Lasertechnik GmbH, Austria) used for Cy7.5 excitation are not significantly distorted up to an operating temperature of 40 °C. For the laser diode (PLT5-520B, ams-OSRAM AG, Austria) used for Cy3 excitation, a maximum operating temperature of up to 50 °C is possible without significant distortion of the emission spectra.

When driving laser diodes, some basic rules must be followed. The maximum output power specified by the manufacturer must not be exceeded under any circumstances. Overcurrent or undervoltage, even for a short time, can cause damage or even total failure of the laser diode. Therefore, a laser diode must always be operated with a suitable driver circuit.

Laser diodes behave electrically very similar to light emitting diodes. Laser operation starts above the laser threshold I_{th} (threshold current). Above this threshold, the optical losses in the laser cavity remain the same for all input powers. This results in an almost straight line when the output power P_{o}

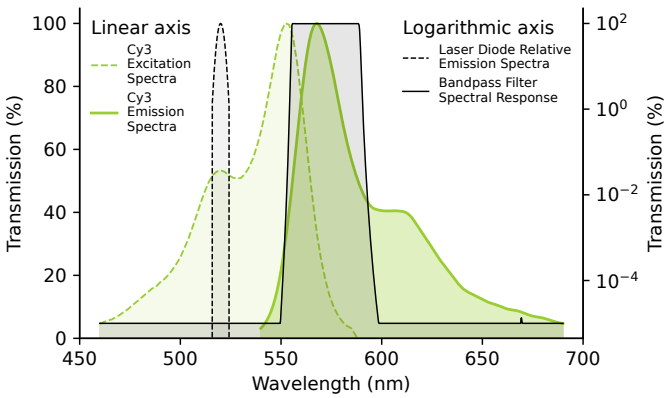

(a) Spectra of dye Cy3, laser diode PLT5-520B and filter FF01-572/28-25.

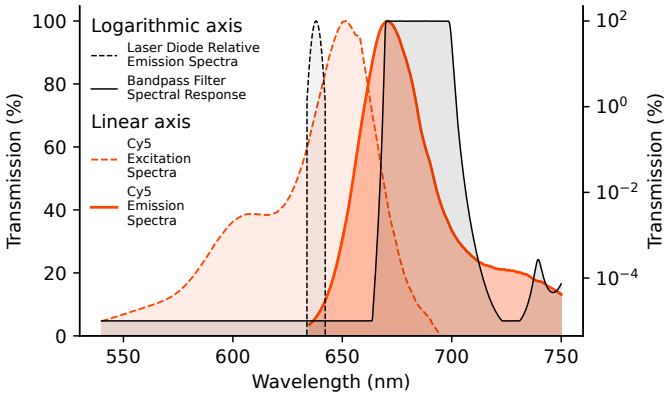

(b) Spectra of dye Cy5, laser diode RLT635-50MGS and filter FF02-684/24-25.

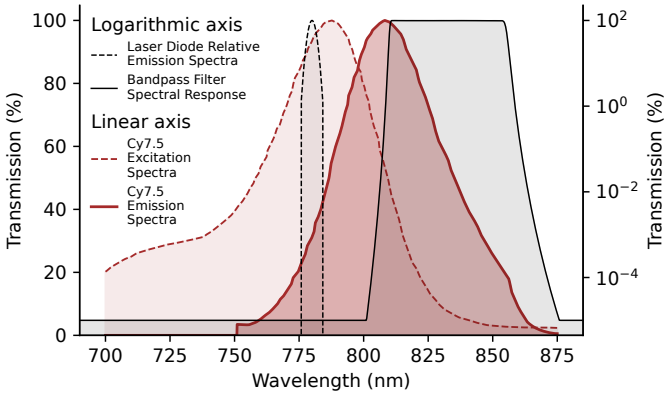

(c) Spectra of dye Cy7.5, laser diode QL78M6SA and filter FF01-832/37-25.

Fig. 1. To capture light as efficiently as possible, the fluorescent label must be excited as close to the excitation peak as possible and the spectral response of the filter must cover as much of the emission band as possible. Fig. 1a, Fig. 1b and Fig. 1c represent the ideal situation. The spectral data are taken from Chroma Spectral Viewer, Semrock MyLight - View and Model Theoretical Data Tool, and the respective laser diode data sheet.

is plotted against the input pump power I (operating current). The slope of this line is called the slope efficiency

$$\eta_{\mathrm{slope}} \approx \frac{P_{\mathrm{o}}}{I - I_{\mathrm{th}}} \quad \text{for } I > I_{\mathrm{th}}. \tag{1}$$

Both the slope efficiency η_{slope} and the threshold current I_{th} of the laser diode are affected by temperature. The threshold current increases with increasing operating temperature, while

the optical output power and slope efficiency decrease. Consequently, temperature changes during operation have a great impact on the stability of the optical output power of a laser diode.

When measuring fluorescence intensity, it is of great importance that the detected light intensity is only affected by changes in marker concentration. Therefore, ensuring a constant optical output power of the laser diode is crucial. Laser diode drivers with automatic power control (APC) are able to keep the output power constant during operation. This control technique uses laser diodes with a feedback path. A monitor diode integrated into the laser diode package provides a photocurrent proportional to the output power. Lasers with integrated monitor diodes are available in N-type, P-type, and M-type configurations and offer three variations for the internal connection between the laser and the monitor diode. The output of an integrated monitor diode is not suitable for calibration. Due to manufacturing tolerances, the monitor current can vary by a factor of 10 for the same output power. Therefore, calibration of the laser output power with an external optical power meter is required. The APC laser diode driver (iC-NZN, iC-Haus, Germany) is a highly integrated driver solution equipped with several safety measures, such as laser current limiting, error signal output, and safety shutdown options. The minimum operating circuit requires only two external resistors to set the nominal and limit laser current. The nominal laser current is set by a potentiometer, allowing easy calibration of the output power. In addition, the iC-NZN is capable of driving laser diodes with high forward voltages, providing a versatile and compact driver solution.

The proposed excitation path is similar to the bright-field illumination geometry used in optical microscopy [17]. Unlike the commonly used inline illumination, no dichroic filter is required because the excitation and emission paths are optically isolated from each other. The most important goal of the excitation path is to ensure a uniformly illuminated detection area. The output of edge-emitting laser diodes is asymmetric, the perpendicular $\Theta_\perp$ (major) beam divergence is larger than the parallel $\Theta_\parallel$ (minor). This asymmetry results in an elliptical beam when the light propagates. Therefore, the position of the laser diode is chosen so that an artificial round beam with the minor divergence angle can illuminate the measurement area. To counteract the nearly Gaussian intensity profile of the laser beam, an optical diffuser is placed in front of the laser diode. Although this setup cannot guarantee a completely uniform illumination of the measurement area, it offers a viable alternative to conventional solutions due to its simple, space-saving and cost-effective design.

The desired position of the laser diode is best determined using the laws of paraxial refraction and coordinate transformation. A two-dimensional representation of the optical setup is sufficient and simplifies the calculations. In addition, the beam refraction (angular range) of the diffuser must not be neglected.

The area illuminated by one laser diode is described by the two points P_n (near) and P_f (far). They mark the outermost points where the emitted light of the laser diode impinges on the measurement area. The origin of the global coordinate system with axes x and y is in the center of the measurement area. Note that the points P_n and P_f are not symmetrical with respect to the global origin. This creates a region where only light from one laser diode is incident. Consequently, the point P_n of both laser diodes (left and right) must be at least 15 mm away from the global origin when they impinge on the measurement surface, so that the circular measurement area with a diameter of 30 mm is illuminated by both beams. The orientation of a laser diode, with respect to the x-axis, is described by the angle

$$\phi = \arctan\left(\frac{y_\mathrm{ld}}{x_\mathrm{ld}}\right), \tag{2}$$

where x_ld and y_ld define the position of the laser diode in the global coordinate system. Equation (2) fixes the propagation axis of the laser diode beam to the center of the measurement area. The lines L_n and L_f describe the envelope of the emitted laser beam before passing through the diffuser. The envelope can be represented by x_n and x_f, the x-axis of the two local coordinate systems with the origin at x_ld and y_ld. For better readability, the coordinate systems for calculating P_f are not shown in Fig. 2. The coordinate systems for calculating P_f are the mirror images of those needed for the calculation of P_n with respect to the propagation axis of the laser beam. The two points P_n and P_f lie on the intersection between the x-axis and x_nd and x_fd, respectively. A simple way to calculate the intersection is to transform the global coordinate system to represent either one of the ray envelopes L_nd or L_fd. For the x-axis of the global system to represent x_nd, two transformations are required. First, its origin must be moved to the point x_ld and y_ld, also the x-axis must be rotated by an angle of $\phi+\Theta_\parallel/2$. The transformation matrix

$$T_\mathrm{ld} = \begin{bmatrix} \cos(\phi+\Theta_\parallel/2) & -\sin(\phi+\Theta_\parallel/2) & x_\mathrm{ld} \\ \sin(\phi+\Theta_\parallel/2) & \cos(\phi+\Theta_\parallel/2) & y_\mathrm{ld} \\ 0 & 0 & 1 \end{bmatrix} \tag{3}$$

transforms the global system into the coordinate system of the laser diode with its axis x_n and y_n. For the axis x_n of the laser diode system to represent x_nd, the transformation matrix

$$T_\mathrm{di} = \begin{bmatrix} \cos(\Theta_\mathrm{D}/2) & -\sin(\Theta_\mathrm{D}/2) & L_\mathrm{n} \\ \sin(\Theta_\mathrm{D}/2) & \cos(\Theta_\mathrm{D}/2) & 0 \\ 0 & 0 & 1 \end{bmatrix} \tag{4}$$

is needed. The displacement in T_di is the distance (in the laser diode coordinate system) between the laser diode and the diffuser, represented by L_n. Also, a rotation of x_n by half of the spatial range of the diffuser Θ_D is necessary to transform x_n to x_nd. Both transformations can be combined by multiplying T_ld by T_di, resulting in a single transformation matrix T_Pn. The only difference in the transformation matrix T_Pf, which transforms the x-axis of the global coordinate system to x_fd (L_fd), is the rotation around the negative of the angles $\Theta_\parallel/2$ in T_ld, $\Theta_\mathrm{D}/2$ in T_di and the substitution of L_n by L_f in T_di.

By adding the bottom row to the transformation matrix, i.e., transforming the problem to a higher order dimension, the problem can be formulated exclusively as a series of matrix multiplications. This has advantages, such as adding any number of rotations, translations or scaling sequences,

Conference ID: 1570790231

while still allowing the problem to be represented by a single transformation matrix.

To find the two intersection points and thus the two points P_n and P_f, one has to solve the system of equations

$$\begin{bmatrix} P_\mathrm{n} \\ 0 \\ 1 \end{bmatrix} = T_\mathrm{Pn} \cdot \begin{bmatrix} P_{\mathrm{n_n}} \\ 0 \\ 1 \end{bmatrix} \tag{5}$$

or

$$\begin{bmatrix} P_\mathrm{f} \\ 0 \\ 1 \end{bmatrix} = T_\mathrm{Pf} \cdot \begin{bmatrix} P_{\mathrm{f_f}} \\ 0 \\ 1 \end{bmatrix} \tag{6}$$

where $P_{\mathrm{n_n}}$ and $P_{\mathrm{f_f}}$ are the transformed representations of P_n and P_f. The second entry in the vectors in (5) and (6) corresponds to the y-axis of the respective coordinate system. In both cases, this is set to zero since the points P_n and P_f lie on the x-axis in both systems. The equations (5) and (6) can be rewritten as

$$\begin{cases} P_\mathrm{n} & = T_{\mathrm{Pn}_{1,1}} \cdot P_{\mathrm{n_n}} + T_{\mathrm{Pn}_{1,3}} \\ 0 & = T_{\mathrm{Pn}_{2,1}} \cdot P_{\mathrm{n_n}} + T_{\mathrm{Pn}_{2,3}} \\ 1 & = 1 \end{cases} \tag{7}$$

or

$$\begin{cases} P_\mathrm{f} & = T_{\mathrm{Pf}_{1,1}} \cdot P_{\mathrm{f_f}} + T_{\mathrm{Pf}_{1,3}} \\ 0 & = T_{\mathrm{Pf}_{2,1}} \cdot P_{\mathrm{f_f}} + T_{\mathrm{Pf}_{2,3}} \\ 1 & = 1 \end{cases}, \tag{8}$$

here the indices $T_{\mathrm{column,row}}$ describe the respective element in the transformation matrix T_Pn or T_Pf. Substituting $P_{\mathrm{n_n}}$ from the first row with the second row, allows to rewrite the set of equations in (7) as

$$P_\mathrm{n} = T_{\mathrm{Pn}_{1,1}} \cdot \frac{-T_{\mathrm{Pn}_{2,3}}}{T_{\mathrm{Pn}_{2,1}}} + T_{\mathrm{Pn}_{1,3}}. \tag{9}$$

The same substitution in (8) leads to

$$P_\mathrm{f} = T_{\mathrm{Pf}_{1,1}} \cdot \frac{-T_{\mathrm{Pf}_{2,3}}}{T_{\mathrm{Pf}_{2,1}}} + T_{\mathrm{Pf}_{1,3}}. \tag{10}$$

The area illuminated by one laser diode is described by the parametric representation of a circle

$$\begin{aligned} x &= h + r \cdot \cos(\alpha) \\ z &= r \cdot \sin(\alpha) \end{aligned} \tag{11}$$

which describes each point on the perimeter as a function of radius r and angle α, where $0 \leq \alpha \leq 2\pi$, as shown in Fig. 2. The radius r is calculated by

$$r = \frac{|P_\mathrm{n}| + |P_\mathrm{f}|}{2}. \tag{12}$$

The center point $(h, 0)$ is defined by

$$h = \frac{P_\mathrm{n} + P_\mathrm{f}}{2}. \tag{13}$$

To calculate the area illuminated by the second laser diode, the result of (13) must be mirrored on the y-axis of the global coordinate system. The mirrored center point is inserted into (11) to calculate the illumination of the second laser diode. Accurate illumination is achieved when the circular measurement area with a diameter of 30 mm fits into the plane illuminated by both laser diodes. This method allows easy estimation of appropriate laser diode positions, which was important during the design process and allowed quick and easy evaluation of changes.

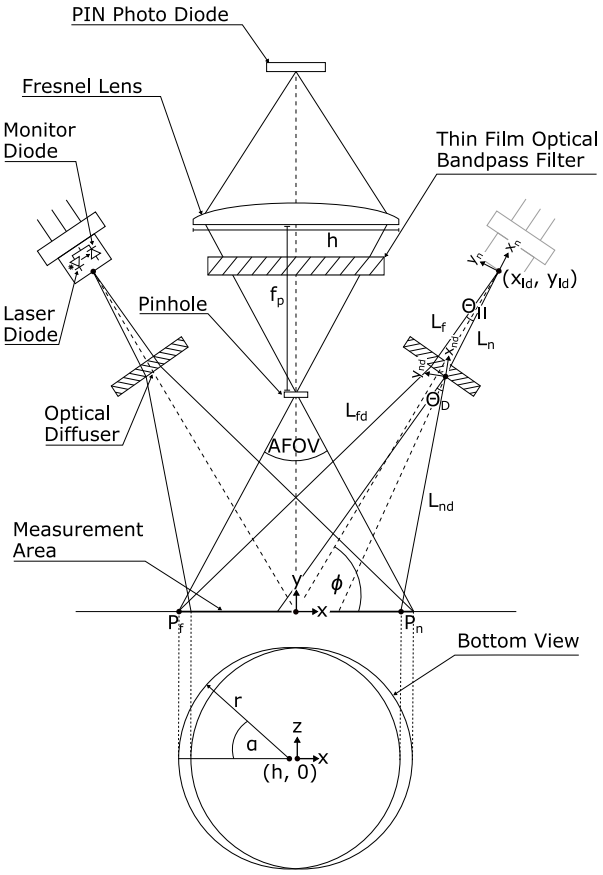

Fig. 2. Schematic representation of the optics integrated into the fluorescence intensity meter. Two laser diodes, located on either side, excite the fluorescent labels by illuminating them with monochromatic light. An optical diffuser is placed in front of each laser diode to ensure uniform illumination of the measurement area. A pinhole is used to limit the AFOV along with the angle of incidence at which the light rays pass through the filter. This ensures reliable separation of excitation and emission. A Fresnel lens focuses the light onto a PIN photodiode, which converts the incident light into an electrical signal.

B. Emission

The emission path is responsible for separating the excitation of the laser diode from the emission of the marker and focusing it on a detector. This separation depends on an appropriately selected optical filter. To capture as much fluorescent light as possible, the spectral response of the filter should cover most of the emission band of the marker. Fig. 1 shows a suggested selection of a thin-film filter under ideal conditions, where the light is incident at a normal angle, for the fluorescent dyes Cy3, Cy5, and Cy7.5. In reality, filters often operate in systems where the light is incident at a non-normal angle. A distinction is made between the angle of incidence (AOI) for collimated light and the cone half angle (CHA) for non-collimated light.

When light is incident at a non-zero AOI, the optical path lengths through the media or the phase thickness in a multilayer coating change. This leads to an angle-dependent shift in

Conference ID: 1570790231

wavelength where constructive and destructive interference occur, i.e.

$$\lambda_{(\theta)} = \lambda_0 \frac{\sqrt{n_{\text{eff}}^2 - \sin^2\theta}}{n_{\text{eff}}}, \tag{14}$$

where n_{eff} describes the effective refractive index of the multilayer thin film coating, θ the angle of incidence, λ_0 the spectrum at normal incidence, and $\lambda_{(\theta)}$ the distorted spectral response of the filter at an AOI greater than zero. The filter spectrum is distorted at higher AOI and shifts the spectral transmission to shorter wavelengths. This distortion and blue shift of the filter spectrum is unique to each filter design. For the filters selected for the multi-wavelength fluorescence measurement device, it was determined that the AOI should not exceed 15 °. At a larger AOI, the spectral response of the filter undergoes a blue shift to such an extent that reliable separation of laser diode excitation and marker emission is no longer assured. A similar effect is caused by CHA, which is often considered to average the AOI effects over a range of different angles [18]. Limiting the AOI to a maximum of 15 ° is equivalent to limiting the angular field of view (AFOV) to 30 °. In the emission path of the instrument, this is achieved by a simple pinhole design. Trigonometrically, the AFOV can be expressed as follows

$$\text{AFOV} = 2 \cdot \arctan\left(\frac{h}{2f_{\text{p}}}\right), \tag{15}$$

where h is the height of the image plane and f_{p} is the focal length. At the image plane, a Fresnel lens focuses the incident light onto the PIN photodiode, as shown in Fig. 2.

C. Sensing

To measure fluorescence intensity, the circular detection area of the instrument is placed on the ratiometric fluorescence tattoo sample. The sample is excited with a light pulse at regular intervals so that foreground and background light are alternately detected. By subtracting the background from the foreground light, the actual emission of the marker is obtained, which is represented by the measured photocurrent. The measurement results are shown on the instrument display along with various operating parameters.

For the foreground and background measurements, the photodiode (BPW34S-Z, ams-OSRAM AG, Austria) converts the incident light into a photocurrent. The photocurrent is then integrated by a precision switched-integrator transimpedance amplifier (IVC102, Texas Instruments, USA), which uses a switched-input measurement technique. The block diagram of the measurement circuit is shown in Fig. 3a. This method allows continuous integration of the photocurrent over a defined period of time. The IVC102 holds the output voltage constant (hold period) after integration to ensure stable conversion. During the short hold period, each signal current generated by the sensor charges the source capacitance of the sensor. After the hold and reset sequence, this charge is transferred to the integrator capacitor C_{INT}. Thus, no charge generated by the sensor is lost during the conversion and the input current is continuously integrated. When the laser diodes remain active

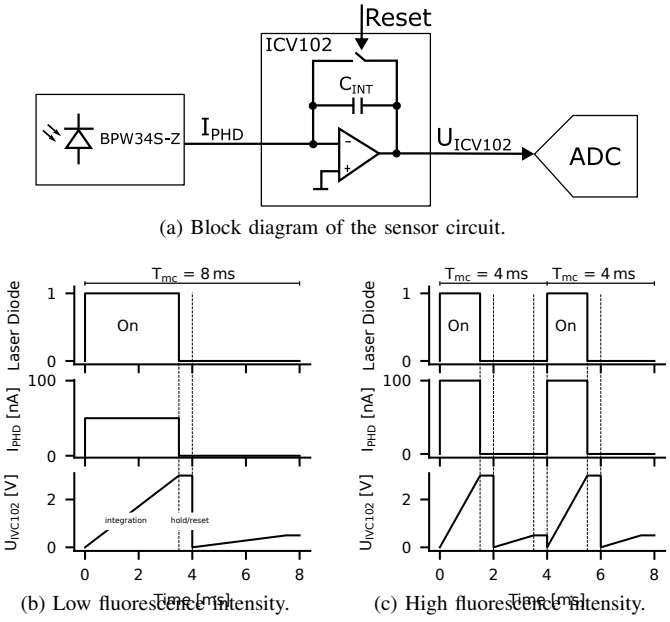

(a) Block diagram of the sensor circuit.

(b) Low fluorescence intensity.

(c) High fluorescence intensity.

Fig. 3. The measurement process is composed of the acquisition of foreground and background light. The foreground cycle measures the light emitted by the marker along with the background noise. The background cycle measures only the intensity of the background signal. The actual fluorescence emission is determined by subtracting the background from the foreground light. The instrument adjusts the measurement time T_{mc} depending on the fluorescence intensity to ensure that the full-scale range of the ADC is never exceeded.

during hold and reset, the source capacitance of the sensor is charged. At the beginning of the background integration phase, these charges are transferred into the integrator capacitor C_{INT} and unintentionally increase the output voltage. As a result, the overall fluorescence intensity measurement is distorted. Therefore, real-time control of the laser diode and integrator is required, i.e., precise timing of the pins of the microcontroller (STM32F072CBT6, STMicroelectronics, Switzerland) used to control the laser diode drivers and integrator. This is achieved by setting the 16-bit hardware timer (TIM17) of the microcontroller to the specified integration time. The timer triggers an interrupt that forces the microcontroller to suspend all other processes and either set or reset the control pins at the exact time specified by the timer. The timer specification, and thus the timing errors for the integration time, are defined by the characteristics of the main clock source (ABL-8.000MHZ-B1U, Abracon, USA) with a frequency stability of ±10 ppm in an operating temperature window of −20 °C ∼ +70 °C. Since the measurement result is directly proportional to the integration time, the errors caused by timing are estimated to be less than 20 ppm. A measurement cycle with its integration, hold, and reset phases can be seen in Fig. 3b and Fig. 3c. During the hold phase, the analog-to-digital converter (ADC) samples the output voltage U_{IVC102}. If it exceeds or does not fully utilize the dynamic range of the ADC, the measurement cycle time is automatically adjusted. The full measurement cycles with variable T_{mc} are shown in Fig. 3. This algorithm averages over several periods and calculates the average photocurrent, standard deviation, and signal-to-noise ratio. All these parameters as well as the measurement duration, the number of averaged samples and the utilization

 Conference ID: 1570790231

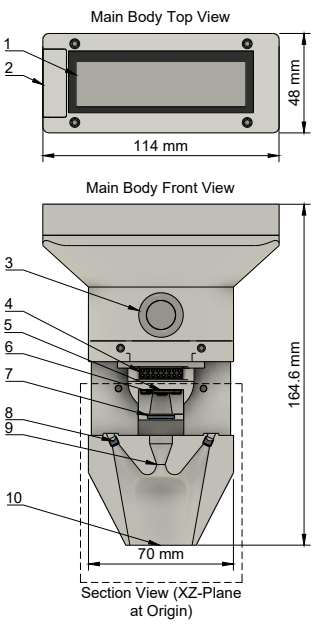

(a) Top view and front view of the main body of the meter. In the lower part of the front view, the device is cut along the xz-plane in the middle of the measurement area marked by the box with the dashed line. 1) Blue OLED matrix display 256x64, 2) Service port (firmware update, debugging), 3) Push button (measurement trigger), 4) Spring loaded connection interface between main body and marker module, 5) Precision transimpedance amplifier with switched integrator U_{IVC102}, 6) Photodiode BPW34S-Z, 7) Fresnel focusing lens, 8) Optical diffuser, 9) Pinhole, 10) Measurement area.

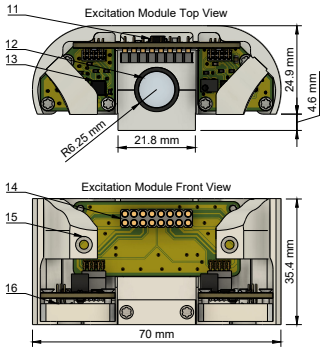

(b) Top view and front view of the marker module. 11) NVRAM chip for storing module information, 12) Marker emission filter, 13) iC-Haus NZN laser diode driver, 14) Receptacle for connection between main body and marker module, 15) Threaded inserts for safety screws to fix the module, 16) Aluminum heat sink.

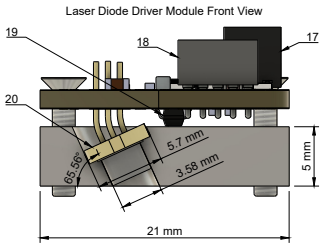

(c) Front view of the laser diode driver module. 17) Potentiometer for adjusting the optical output power of the laser diode, 18) Connection interface to receptacle board, 19) Digital temperature sensor, 20) Laser diode.

Fig. 4. View of the portable multi-wavelength fluorescence meter, marker module and laser diode driver. The upper part of the instrument contains the display, the main electronics, and the measurement trigger. The lower part consists of the measuring head, the optical diffusers, the focusing lens and the photodetection module. The marker modules are fixed with two locking screws. The entire housing and the marker modules are 3D printed using FDM technology.

of the dynamic range of the ADC are shown on the display after each measurement.

D. Housing

The multi-wavelength fluorescence meter consists of the main body and interchangeable marker modules. The main body houses the electronics and the display, the middle part contains the measurement trigger (push button), the detection unit and the electrical connection interface for the marker modules, the lower part contains the optical diffusers. The front view of the device is shown in Fig. 4a. The narrow middle part of the instrument allows one-handed operation. The meter can be held in the middle part below the display. A measurement is triggered by pressing the push button.

The exchangeable marker modules are the central element of the developed fluorescence measurement system. Depending on which fluorescence marker is to be measured, an appropriate module must be inserted into the instrument. A marker module houses an emission filter, the two laser diode driver modules, the laser diodes with custom heat sinks and the connection unit, as shown in Fig. 4b. The heat sink, made of aluminum, increases the runtime of each laser diode before it reaches its maximum operating temperature. The heat sink also serves as a holder for the laser diode (TO56 package) and the driver module. The driver unit is screwed into the aluminum block with two Torx T5 screws. The heat sink is stamped from a 5 mm thick aluminum plate purchased from Blexon AG. It has a length of 21 mm and a width of 11 mm. In each heat sink, a 3.6 mm diameter trough hole and a 5.7 mm diameter blind hole are drilled in the aluminum block at an angle of 65.56 ° to the surface of the measurement area, which serve as a mount for the laser diode. The angle of 65.56 ° is based on the calculations in section II-A. For the PLT5-520B laser diode with a minimum parallel beam divergence $\Theta_{\parallel} = 5.5$ ° (smallest parallel beam divergence of the three laser diodes used, represents the worst case), a position of $x_{\mathrm{ld}} = 25.4$ mm, $y_{\mathrm{ld}} = 55.6$ mm, the distance $L_{\mathrm{n}} = 6$ mm, and a minimum diffuser angle range of $\Theta_{\mathrm{D}} = 24$ ° is sufficient to illuminate the measurement area and fits well within the dimensions of the device. Two 2.5 mm diameter holes are drilled perpendicular to the top plane and serve as driver mounts. For a detailed illustration of the heat sink and driver module, see Fig. 4c. Each module contains a memory chip that stores all relevant information such as the module identification, production date, laser diode type, nominal emission wavelength, nominal optical output power, maximum laser diode operating temperature, laser diode forward voltage, and recommended marker emission filter. When the excitation module is inserted, the measurement system reads the memory and automatically programs the drivers and the laser diode's internal power supply (maximum 10 V) to the required specifications. The holder for the marker emission filter in the excitation module supports optical filters with a diameter of 12.7 mm and a maximum height of 6 mm. These filters should be selected according to the marker to be measured and complementary to the laser diodes. They should meet the requirements described in the sections II-A and II-B.

The entire housing was printed on a Prusa i3 MK3S using FormFutura's Stealth Black PLA filament (matte black with a rough surface). The PrusaSlicer with Prusa's standard preconfigured print settings for PLA with a print quality of 0.1 mm was used to create the G-code. The printer is equipped with the standard E3D V6 HotEnd and a 0.4 mm steel nozzle.

III. Empirical Evaluation

A. Preparation of the Skin Phantoms

The Sylgard 184 silicone elastomer kit (Dow Corning) was purchased from Swiss-composite.ch (Suter-Kunststoffe AG, Switzerland). The kit contains the polydimethylsiloxane (PDMS) monomer and the curing agent. A mixture of the monomer and the curing agent in a 10:1 ratio was used to prepare the PDMS skin phantom. The PDMS is cured for at least 48 h at room temperature to allow the droplet encapsulation process. Glycerol (Rotipuran > 86%, CAS No: 56-81-5) and dye ICG (Indocyanine green, Cardiogreen, CAS

This article has been accepted for publication in IEEE Transactions on Instrumentation and Measurement. This is the author's version which has not been fully edited and content may change prior to final publication. Citation information: DOI 10.1109/TIM.2023.3270999 Conference ID: 1570790231

(a) Measurement device placed on the Cy5 marker embedded in the skin phantom.

(b) Liquid Cy5 dye droplet embedded in the clear PDMS skin phantom.

(c) A 500 μm thick layer of rat skin placed over the marker droplet.

Fig. 5. Experimental setup to study the effects of skin thickness on fluorescence measurements. Rat skin of either 500 μm or 1 mm thickness was placed over the dye droplets on the surface of the skin phantoms. The instrument is placed so that only one marker droplet is within the measurement zone and thus only the fluorescence intensity of that droplet is measured.

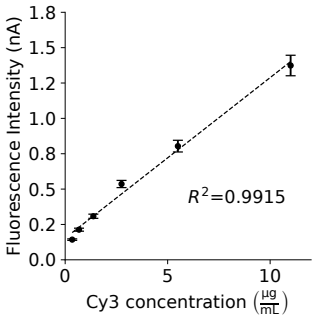

(a) Dilution series and measurement results for the fluorescent dye Cy3.

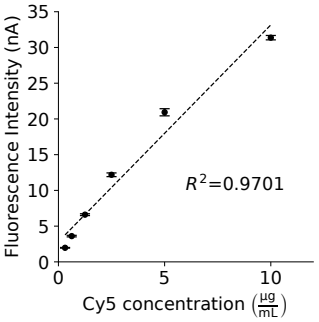

(b) Dilution series and measurement results for the fluorescent dye Cy5.

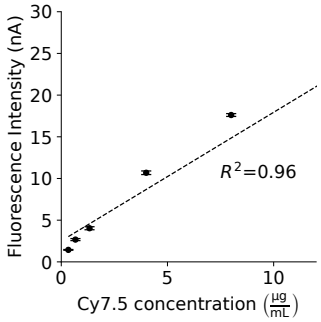

(c) Dilution series and measurement results for the fluorescent dye Cy7.5.

Fig. 6. The meter shows good correlation for all three fluorescent dyes tested. At similar marker concentrations, the measured intensity values of Cy3 in Fig. 6a are a factor of 20 smaller than those of Cy5 and Cy7.5 in Fig. 6b and Fig. 6c, respectively. This difference in intensity is still under investigation. However, it illustrates the sensitivity of the instrument over a wide dynamic range. The round markers represent the mean values, and the error bars represent the standard deviation for each set of measurements.

No: 3599-32-4) were purchased from Carl Roth (Switzerland) to prepare the solutions. The Cy3 and Cy5 dyes were synthesized following a protocol previously described in [3]. Cy3, Cy5, and ICG dye solutions were prepared by adding a few mg of dye powder to glycerol (5 ml for stock solution) and diluting sequentially. Six concentrations were established for each dye. Then, one drop (60 μl) of each solution was added to the unpolymerized PDMS matrix, which was poured into a plastic mold [19]. The skin phantoms were cured for several hours until the polymer solidified and the liquid dye droplets were encapsulated. The skin phantom with the 6 concentrations of Cy5 droplets is shown in Fig. 5.

B. Experimental Setup

For the intended measurement task, monitoring the intensity of a fluorescent marker over time, the linearity of the system is crucial. The validation performed focuses on observing linearity rather than calibrating to absolute intensity values. Dilution series were prepared in ethanol for the fluorescent markers Cy3, Cy5, and Cy7.5 to collect preliminary data on the performance of the fluorescence intensity meter. Measurements were repeated several times for each dilution series. To test the effect of marker injection depth (thickness of skin tissue) on fluorescence measurements, rat skin with a thickness of either 500 μm or 1 mm was placed over the dye drops on the surface of the skin phantoms. Then, the fluorescence intensity was measured for all dyes. The experimental setup is shown in Fig. 5.

C. Results

The results of the linearity measurements are shown in Fig. 6. The intensity measured by the device shows linear behavior with respect to concentration for all three fluorescent dyes tested. However, it is noticeable that at similar marker concentrations, the fluorescence intensity values for the Cy3 dilution series are lower by a factor of 20, as shown in Fig. 6a. Although these significantly lower values compared to Cy5 and Cy7.5 are not yet fully elucidated and require further investigation, this highlights the high sensitivity of the instrument over a wide dynamic range. These initial measurements indicate a sensitivity range large enough to measure signals in the pico-ampere range. In particular, the use of this instrument has been validated in vivo for measuring microneedle-based fluorescence tattoos for physiological monitoring applications [3]. In a previous study, a similar single-wavelength portable fluorescence meter was compared to a commercially available fluorescence microscope. This showed sufficient sensitivity for evaluation of dermal clearance [20]. The same device was also clinically validated [21].

The data in Fig. 7 show that the signal intensity decreases significantly as a function of skin thickness. The signal intensity decreases to about 45% for the Cy5 and ICG markers after a 500 μm thick skin layer is added. The fluorescence intensity of Cy3 decreases to 37% under the same conditions. When 1 mm thick skin tissue covers the marker, the signal intensities of Cy3, Cy5, and ICG decrease to 8%, 25%, and 15%, respectively, compared with no skin. This decrease in fluorescence intensity was greater for Cy3 (lower wavelength) than for Cy5 and ICG (higher wavelength), illustrating the better transmission of red and near-infrared light through the skin compared with light

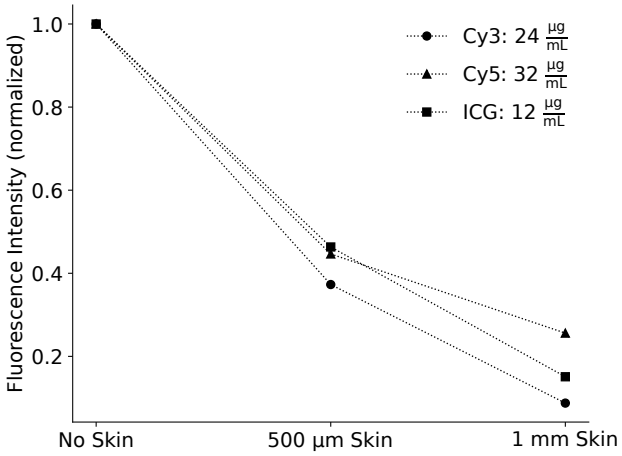

Fig. 7. Fluorescence intensity decreases significantly when skin tissue is placed over the sample. Signal intensity decreases to about 45% for the Cy5 and ICG markers after a 500 μm thick skin layer is added. The fluorescence intensity of Cy3 decreases to 37% under the same conditions. When 1 mm thick skin tissue covers the marker, the signal intensities of Cy3, Cy5, and ICG decrease to 8%, 25%, and 15%, respectively, compared with no skin. Longer wavelengths allow deeper absorption, so the excitation for Cy5 and ICG is higher than for Cy3. This suggests that markers with longer excitation and emission wavelengths also provide better signals in deeper skin layers. In addition, the data suggests that measurements of absolute marker concentrations would not provide additional value because fluorescence intensity is highly dependent on the thickness of the overlying skin layer.

at lower wavelengths.

IV. Conclusion

The goal of this work was to develop a portable and inexpensive fluorescence meter that can operate at multiple wavelengths. The optical components were reduced to the essentials to allow for a simplified and compact instrument design. The precision switched integrator transimpedance amplifier and variable measurement time provide high sensitivity over a wide dynamic range, even though a simple PIN photodiode detector is used. With its interchangeable fluorescence modules, the instrument can be adapted to different fluorescence intensity measurement tasks, which is a first in this compact form and with this level of sensitivity. Test series with the Cy3, Cy5 and Cy7.5 markers demonstrate the great versatility. The device offers a portable, cost-effective and adaptable fluorescence measurement system that can be coupled with non-invasive fluorescence sensors. It enables intradermal administration for quantitative monitoring of physiological and pathological parameters remotely, without the need for trained personnel and complex instrumentation. For example, the use of this technology has recently been demonstrated for non-invasive monitoring of skin inflammation [3]. It will therefore be of great help to researchers and clinicians working with dermally injected fluorescent tracers.

References

[1] S. S. Gambhir, T. J. Ge, O. Vermesh, and R. Spitler, "Toward Achieving Precision Health," *Science Translational Medicine*, vol. 10, p. eaao3612, Feb. 2018.

[2] F. R. Beyette, C. A. Gaydos, G. J. Kost, and B. H. Weigl, "Point-of-Care Technologies for Health Care," *IEEE transactions on bio-medical engineering*, vol. 58, pp. 732–735, Mar. 2011.

[3] S. Babity, F. Couture, E. V. R. Campos, S. Hedtrich, R. Hagen, D. Fehr, M. Bonmarin, and D. Brambilla, "A Naked Eye-Invisible Ratiometric Fluorescent Microneedle Tattoo for Real-Time Monitoring of Inflammatory Skin Conditions," *Advanced Healthcare Materials*, vol. 11, p. 2102070, Mar. 2022.

[4] K. Tsubokura, K. K. H. Vong, A. R. Pradipta, A. Ogura, S. Urano, T. Tahara, S. Nozaki, H. Onoe, Y. Nakao, R. Sibgatullina, A. Kurbangalieva, Y. Watanabe, and K. Tanaka, "In Vivo Gold Complex Catalysis within Live Mice," *Angewandte Chemie International Edition*, vol. 56, pp. 3579–3584, Mar. 2017.

[5] A. Bigdeli, F. Ghasemi, S. Abbasi-Moayed, M. Shahrajabian, N. Fahimi-Kashani, S. Jafarinejad, M. A. Farahmand Nejad, and M. R. Hormozi-Nezhad, "Ratiometric Fluorescent Nanoprobes for Visual Detection: Design Principles and Recent Advances - A Review," *Analytica Chimica Acta*, vol. 1079, pp. 30–58, Nov. 2019.

[6] R. M. Sánchez-Martín, M. Cuttle, S. Mittoo, and M. Bradley, "Microsphere-Based Real-Time Calcium Sensing," *Angewandte Chemie (International Ed. in English)*, vol. 45, pp. 5472–5474, Aug. 2006.

[7] W. Lin, L. Yuan, W. Tan, J. Feng, and L. Long, "Construction of Fluorescent Probes via Protection/Deprotection of Functional Groups: A Ratiometric Fluorescent Probe for Cu2+," *Chemistry (Weinheim an Der Bergstrasse, Germany)*, vol. 15, no. 4, pp. 1030–1035, 2009.

[8] Z.-h. Xu, H.-w. Wang, X.-f. Hou, W.-l. Xu, T.-c. Xiang, and C.-z. Wu, "A Novel Ratiometric Colorimetric and NIR Fluorescent Probe for Detecting Cu2+ with High Selectivity and Sensitivity Based on Rhodamine-Appended Cyanine," *Sensors and Actuators B: Chemical*, vol. 201, pp. 469–474, Oct. 2014.

[9] A. Tofighi Zavareh, B. Ko, J. Roberts, S. Elahi, and M. J. Mcshane, "A Versatile Multichannel Instrument for Measurement of Ratiometric Fluorescence Intensity and Phosphorescence Lifetime," *IEEE Access*, vol. 9, pp. 103835–103849, July 2021.

[10] U. Obahiagbon, D. Kullman, J. T. Smith, B. A. Katchman, H. Arafa, K. S. Anderson, and J. B. Christen, "Characterization of a Compact and Highly Sensitive Fluorescence-Based Detection System for Point-of-Care Applications," in *2016 IEEE Healthcare Innovation Point-Of-Care Technologies Conference (HI-POCT)*, pp. 117–120, 2016.

[11] A. Huttunen, S. Aikio, M. Kurkinen, J.-T. Mäkinen, R. Mitikka, L. Kivimaki, M. Harjumaa, J. Takalo-Mattila, C. Liedert, J. Hiltunen, and L. Hakalahti, "Portable Low-Cost Fluorescence Reader for LFA Measurements," *IEEE Sensors Journal*, vol. 20, pp. 10275–10282, May 2020.

[12] M. V. Gorbunova, P. Y. Evstigneeva, V. V. Apyari, and S. G. Dmitrienko, "A Monitor Calibrator as a Portable Tool for Determination of Luminescent Compounds," *IEEE Transactions on Instrumentation and Measurement*, vol. 70, pp. 1–10, 2021.

[13] A. Samorè, M. Rusci, D. Lazzaro, P. Melpignano, L. Benini, and S. Morigi, "BrightNet: A Deep CNN for OLED-Based Point of Care Immunofluorescent Diagnostic Systems," *IEEE Transactions on Instrumentation and Measurement*, vol. 69, pp. 6766–6775, Sept. 2020.

[14] R. S. Sengar, A. K. Upadhyay, and B. Jain, "Deep Learning Aided Small-Sized Portable Fluorescence Biochip Reader," *IEEE Transactions on Instrumentation and Measurement*, vol. 71, pp. 1–9, 2022.

[15] R. Hagen, D. Fehr, F. Spano, D. Brambilla, and M. Bonmarin, "Portable Multi-Wavelength Fluorescence Measurement Device," in *2022 IEEE International Symposium on Medical Measurements and Applications (MeMeA)*, pp. 1–6, June 2022.

[16] J. R. Lakowicz, *Principles of Fluorescence Spectroscopy*. Boston, MA: Springer, 3rd ed., 2006.

[17] R. Wegerhoff, O. Weidlich, and M. Kässens, "Basics of Light Microscopy & Imaging." GIT Verlag, June 2006.

[18] R. A. Crocombe, P. E. Leary, and B. W. Kammrath, *Portable Spectroscopy and Spectrometry I: Technologies and Instrumentation*. Apr. 2021.

[19] G. Faccio, A. Cont, E. Mailand, E. Zare-Eelanjegh, R. Innocenti Malini, K. Maniura-Weber, R. M. Rossi, and F. Spano, "Complete Inclusion of Bioactive Molecules and Particles in Polydimethylsiloxane: A Straightforward Process Under Mild Conditions," *Scientific Reports*, vol. 9, p. 17575, Nov. 2019.

[20] A. K. Polomska, S. T. Proulx, D. Brambilla, D. Fehr, M. Bonmarin, S. Brändli, M. Meboldt, C. Steuer, T. Vasileva, N. Reinke, J.-C. Leroux, and M. Detmar, "Minimally-Invasive Method for the Point-of-Care Quantification of Lymphatic Vessel Function," *JCI Insight*, vol. 4, Jan. 2019.

[21] A. Polomska, E. Gousopoulos, D. Fehr, A. Bachmann, M. Bonmarin, M. Detmar, and N. Lindenblatt, "Development and Clinical Validation of the LymphMonitor Technology to Quantitatively Assess Lymphatic Function," *Diagnostics*, vol. 11, p. 1873, Oct. 2021.